Physics of the Earth and Planetary Interiors 277 (2018) 99–112

Contents lists available at ScienceDirect

Physics of the Earth and Planetary Interiors

journal homepage: www.elsevier.com/locate/pepi

Seismic anisotropy in central north Anatolian Fault Zone and its implications on crustal deformation

A. Licciardi[a,*], T. Eken[b], T. Taymaz[b], N. Piana Agostinetti[c], S. Yolsal-Çevikbilen[b]

[a] Geophysics Section, School of Cosmic Physics, Dublin Institute for Advanced Studies, Dublin, Ireland
[b] Department of Geophysical Engineering, Faculty of Mines, Istanbul Technical University, Istanbul, Turkey
[c] Department of Geodynamics and Sedimentology, Faculty of Earth Sciences, Geography and Astronomy, University of Vienna, Vienna, Austria

ARTICLE INFO

Keywords:
Seismic anisotropy
Crustal deformation
Seismology
Receiver function

ABSTRACT

We investigate the crustal seismic structure and anisotropy around the central portion of the North Anatolian Fault Zone, a major plate boundary, using receiver function analysis. The characterization of crustal seismic anisotropy plays a key role in our understanding of present and past deformation processes at plate boundaries. The development of seismic anisotropy in the crust arises from the response of the rocks to complicated deformation regimes induced by plate interaction. Through the analysis of azimuthally-varying signals of teleseismic receiver functions, we map the anisotropic properties of the crust as a function of depth, by employing the harmonic decomposition technique. Although the Moho is located at a depth of about 40 km, with no major offset across the area, our results show a clear asymmetric distribution of crustal properties between the northern and southern blocks, divided by the North Anatolian Fault Zone. Heterogeneous and strongly anisotropic crust is present in the southern block, where complex intra-crustal signals are the results of strong deformation. In the north, a simpler and weakly anisotropic crust is typically observed. The strongest anisotropic signal is located in the first 15 km of the crust and is widespread in the southern block. Stations located on top of the main active faults in the area indicate the highest amplitudes, together with fault-parallel strikes of the fast plane of anisotropy. We interpret the origin of this signal as due to structure-induced anisotropy, and roughly determine its depth extent up to 15–20 km for these stations. Away from the faults, we suggest the contribution of previously documented uplifted basement blocks to explain the observed anisotropy at upper and middle crustal depths. Finally, we interpret coherent NE-SW orientations below the Moho as a result of frozen-in anisotropy in the upper mantle, as suggested by previous studies.

1. Introduction

As an intercontinental dextral strike-slip fault with significant strain localization, the 1600-km-long North Anatolian Fault Zone (NAFZ) represents a major plate boundary between the Eurasian plate in the north and the Anatolian plate in the south. Although collision between the Arabian and Eurasian plates (in the east) was initially thought to be the main driving force for the westward motion of the Anatolian plate (e.g. Dewey and Şengör, 1979), recent advances in high-resolution GPS data have revealed a clear role of the southwest-trending rollback of the Hellenic subduction zone in the south Aegean Sea for the rapid deformation of the Aegean-Anatolian region (e.g. McClusky et al., 2000; Reilinger et al., 2006). In this respect, the deformation history of the rocks at various depth ranges remains enigmatic within the crust and mantle of this complex tectonic setting. A detailed sketch of the Anatolian tectonic setting can be found in Fig. 1.

The determination of the directional dependence of seismic wave speed, also known as seismic anisotropy, plays a fundamental role in the elucidation of the complicated deformation regimes induced by plate interaction along such plate margin.

Crustal seismic anisotropy is generally attributed to the alignment of joints or microcracks, to lattice preferred orientation (LPO) of anisotropic minerals, or to highly foliated metamorphic rocks (e.g., Sherrington et al. 2004). In the upper crust, possible sources of seismic anisotropy can be either stress-induced or structure-induced (Boness and Zoback, 2006). Stress-induced anisotropy can be generated either by the extensive dilatancy of fluid-filled microcracks (Crampin, 1987) or by the preferential closure of fractures by the in situ stress field (Boness and Zoback, 2006). In the latter case, the orientation of fast waves of vertically propagating shear waves aligns parallel to the maximum horizontal stress (SH_{max}). When structure-induced mechanisms are dominant, seismic anisotropy may be associated to the

* Corresponding author at: Géosciences, Université de Rennes 1, Rennes, France.
E-mail address: andrea.licciardi@univ-rennes1.fr (A. Licciardi).

https://doi.org/10.1016/j.pepi.2018.01.012
Received 4 October 2017; Received in revised form 14 December 2017; Accepted 26 January 2018
Available online 06 February 2018
0031-9201/

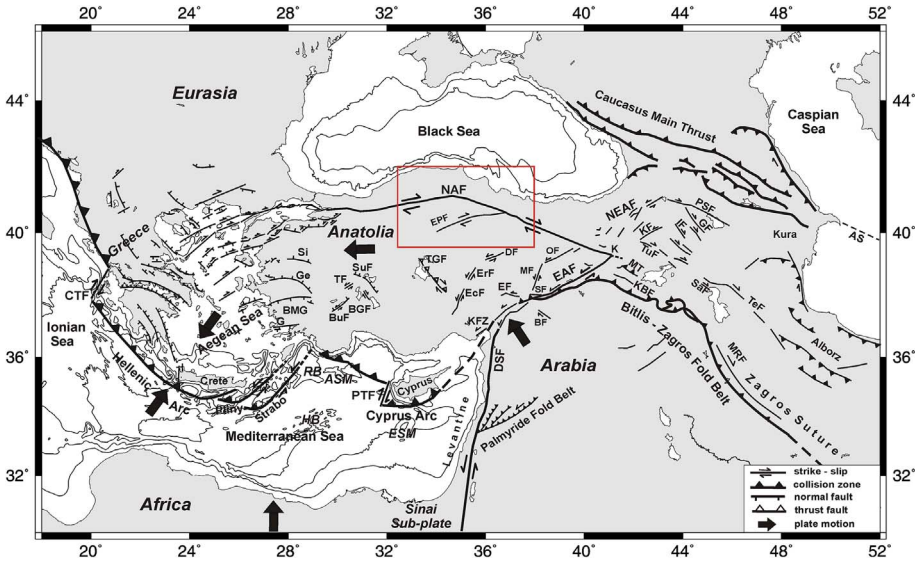

Fig. 1. A sketch map of active tectonic boundaries in the study area and surroundings. For the source of compiled data, please see Taymaz et al. (1990, 1991, 2004, 2007a,b), Yolsal-Çevikbilen and Taymaz (2012) and references therein. Abbreviations: AS: Apşeron Sill, ASM: Anaximander Sea Mountains, BF: Bozova Fault, BGF: Beyşehir Gölü Fault, BMG: Büyük Menderes Graben, BuF: Burdur Fault, CTF: Cephalonia Transform Fault, DSF: Dead Sea Transform Fault, DF: Deliler Fault, EAF: East Anatolian Fault, EcF: Ecemiş Fault, EF: Elbistan Fault, EPF: Ezine Pazarı Fault, ErF: Erciyes Fault, ESM: Eratosthenes Sea Mountains, G: Gökova, Ge: Gediz Graben, GF: Garni Fault, HB: Herodotus Basin, IF: Iğdır Fault, KBF: Kavakbaşı Fault, KF: Kağızman Fault, KFZ: Karataş-Osmaniye Fault Zone, MF: Malatya Fault, MRF: Main Recent Fault, MT: Muş Thrust, NAF: North Anatolian Fault, NEAF: North East Anatolian Fault, OF: Ovacık Fault, PSF: Pampak-Savan Fault, PTF: Paphos Transform Fault, RB: Rhodes Basin, SaF: Salmas Fault, Si: Simav Graben, SuF: Sultandağ Fault, TeF: Tebriz Fault, TF: Tatarlı Fault, TGF: Tuz Gölü Fault. Black arrows exhibit relative plate motions with respect to Eurasia (McClusky et al., 2003; Reilinger et al., 2006).

alignment of macroscopic features due to shear-induced deformation near active faults (Zhang and Schwartz, 1994; Zinke and Zoback, 2000; Tadokoro et al., 2002), sedimentary bedding planes (Kern and Wenk, 1990), and preferred mineral alignments (Sayers, 1994).

Local shear waves splitting analyses, performed over detected micro-seismic earthquakes along various segments of the NAFZ, have indicated a spatial correlation between the fast polarization directions (FPDs) and station distance from the fault (e.g. Tadokoro et al., 2002; Peng and Ben-Zion, 2004; Hurd and Bohnhoff, 2012; Eken et al., 2013). Lateral variations of the FPDs inferred from local shear waves implied the presence of both stress- and structure induced mechanisms causing seismic anisotropy in the upper 8–10 km of the crust. In addition, these local splitting studies have highlighted the structural control of the complex geologic and tectonic environment along the western segments of the NAFZ on the spatial variation of FPDs.

For the deeper part of the crust, i.e. > 20–25 km, several studies have shown that aligned minerals are the most likely cause of anisotropy (Sherrington et al., 2004, and references therein) and that hexagonal anisotropy with a unique slow symmetry axis can explain seventy percent of the observations (Brownlee et al., 2017). In particular, the alignment of micas along the plane of foliation is often the primary cause of bulk anisotropy in this depth range (Sherrington et al., 2004; Audet 2015).

Over the last decade, receiver function (RF) data have been widely used for the characterization of seismic anisotropy. RFs are time series that represent the impulse response of the near receiver structure in terms of P-to-S conversions contained in the P-coda of teleseismic events (Vinnik, 1977; Langston, 1979). After deconvolution of the vertical trace from the horizontal ones, P-to-SV and P-to-SH converted phases are isolated on the Radial (R) and Transverse (T) components of the RFs, respectively. In particular, P-to-SH conversions are generated from the rotation of the energy out of the source-receiver plane induced by anisotropy and/or dipping velocity contrasts at depth (Sherrington et al., 2004; Maupin and Park, 2007; Piana Agostinetti and Chiarabba, 2008; Schulte-Pelkum and Mahan, 2014a). The analysis of the azimuthally varying characteristic of the P-to-S conversions (amplitudes and delay times) can provide robust information about the location of anisotropy at depth (e.g. Rümpker et al., 2014; Licciardi and Piana Agostinetti, 2016). RFs provide complementary depth-dependent information about seismic anisotropy that is difficult to obtain with other common seismological data (e.g. shear wave splitting and surface waves dispersion), since RFs are strongly sensitive to the depth of contrasts in anisotropic properties.

More in detail, the RF harmonic decomposition technique (Bianchi et al., 2010; Park and Levin, 2016) has proven to be effective to quantify seismic anisotropy in various geodynamical settings over the last decade and at different scales of investigation (Piana Agostinetti et al., 2011; Bianchi et al., 2015; Olugboji and Park (2016); Vinnik et al., 2016) including the shallow crust (Licciardi and Piana Agostinetti, 2017; Piana Agostinetti et al., 2017). In particular, RF harmonics have been used to map the depth-dependent distribution of seismic anisotropy in areas of intense crustal deformation, e.g., around the San Andreas Fault (SAF) (Audet 2015), the Tibetan Plateau (Liu et al., 2015), the Cyclades (Cossette et al., 2016), the Canadian Cordillera (Tarayoun et al., 2017) and the Appennines (Bianchi et al., 2010; 2016).

In this work, we analyse RF harmonics using data from the North Anatolian Fault passive seismic experiment ([dataset]Beck and Zandt, 2005; Biryol et al., 2010), in order to delineate the first-order seismic structure of the crust and to map crustal anisotropy as a function of depth. In particular, our main objectives are to elucidate i) orientation and strength of deformation in the crust at various depth ranges ii) how much the strain fields within crust and upper mantle are coupled iii) possible link between lateral variation of crustal anisotropy parameters and existing lithology contrast across the NAF. These results yield insight into the poorly known role of crustal seismic anisotropy in the area.

2. Geological setting of North-Central Anatolia

The study region is located in an important area of orogenic amalgamation of Anatolia, a transition zone between compressional-deformed eastern Anatolia and extensional western Anatolia. There are numerous key structures developed under the complex deformation, such as the Ezine Pazarı – Sungurlu Fault, the İzmir – Ankara – Erzincan (IAESZ) and Intra – Pontide Suture Zones, the İstanbul Zone, the Sakarya Continent, the Central Pontides, the Kırşehir Massif and the Çankırı Basin (Okay and Tüysüz, 1999; Fig. 2). It is reported that some of these structures (e.g., the Istanbul Zone; Şengör, 1979) were parts of Eurasia, while other fragments were separated from the Arabian-African Plate. Görür et al. (1998) further inform that the major basins in Central Anatolia were formed on continental units; i.e., the Sakarya Continent and the Kırşehir Massif adjacent to the suture zones. These structures have significant importance on understanding the tectonic evolution of the region. For example, the İzmir–Ankara–Erzincan suture zone (IAESZ) is a remnant of the Neo-Tethys Ocean and hence consists of ophiolitic units (Rojay, 2013). It separates the Pontides to the north from the Anatolide–Tauride and the Kırşehir blocks to the south

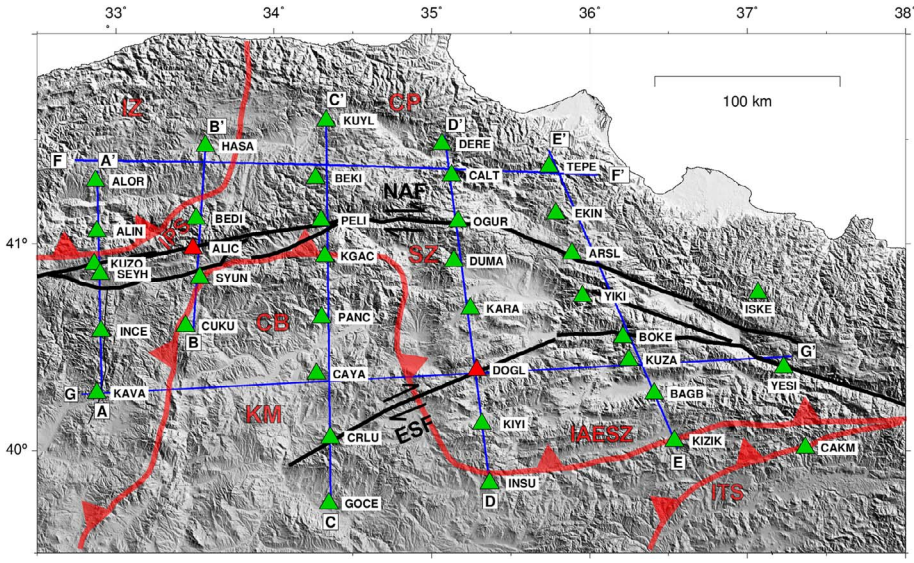

Fig. 2. Map with the location of the 38 broadband seismic stations used in this study. Stations belong to the North Anatolian Fault (NAF) passive seismic experiment (Biryol et al., 2010), which operated from January 2006 to May 2008. Major faults are indicated in black. Suture zones modified after Okay and Tüysüz (1999) are indicated with red lines. Traces of the profiles shown in Fig. 7 are indicated in blue and labelled. Stations used in Figs. 4 and 5 (ALIC and DOGL) are indicated by red triangles. CB, Çankırı Basin; CP, Central Pontides; ESF, Ezinepazari-Sungurlu Fault; IAESZ, Izmir-Ankara-Erzincan Suture Zone; IPS, Intra-Pontide Suture; IZ, Istanbul Zone; ITS, Intra-Tauride Suture; KM, Kırşehir Massif; NAF, North Anatolian Fault;.SZ Sakarya Zone.

(Koçyiğit, 1991; Okay and Tüysüz, 1999; Taymaz et al., 2007a,b). Yolsal-Çevikbilen et al. (2012) identified three major high-velocity blocks in the mid-crust of north-central Anatolia, separated by the İzmir-Ankara-Erzincan Suture Zone, and they interpreted these blocks to be continental basement fragments that were accreted onto the margin, following the closure of Neo-Tethyan Ocean. They also proposed that these high-velocity basement blocks might control the rupture propagations of the historical 1939, 1942 and 1943 earthquakes. Similarly, the Çankırı basin is a natural laboratory for studying the subduction and collision processes, and therefore it is accepted as an essential unit shaping active tectonics of the north-central Anatolia. It locates at the contact region between the Pontides and the Anatolide-Tauride Block, where the 1200 km long North Anatolian Fault Zone bifurcates into a number of small-scale splay faults deforming the Anatolian Block internally, with a complex rotational deformation (Seyitoğlu et al., 2004; Kaymakçı et al., 2009; Lucifora et al., 2013). Recently, Lucifora et al. (2013) have obtained asymmetric tectonic rotations along the opposite edges of the Çankırı Basin from palaeomagnetic data. They have correlated that complex pattern of paleomagnetic rotations with a local block rotation mechanism caused by the strike-slip fault activity along the margins of the Basin.

The other essential tectonic units in north-central Anatolia are the Sakarya Continent and the Kırşehir Massif, also known as the Central Anatolian Crystalline Complex (Akiman et al., 1993). The Kırşehir Massif has a triangular shape that spans over an area of ~300 km × ~200 km (Şengör and Yilmaz, 1981), and is bordered by the right-lateral Tuz Gölü Fault Zone on the west (Çemen et al., 1999) and by the left-lateral strike slip Ecemiş Fault Zone on the east (see Fig. 2). It is also surrounded by ophiolitic melanges associated with subduction-accretion complexes of the Izmir-Ankara-Erzincan and the Inner Tauride suture zones. This Massif is dominated by Late Cretaceous age high-grade metamorphism, intruded by batholiths (Ketin, 1966; Göncüoğlu, 1977; Whitney and Hamilton, 2004). It consists of metamorphic crystalline rocks, i.e., metasediments, ophiolitic sequences, and magmatic intrusions (Kaymakçı et al., 2009). Similarly, the Sakarya Continent has a high-grade metamorphic basement which consists of gneisses, marbles, amphibolites, and metaperidotites, with granodiorite intrusions (Okay, 1996; Görür et al., 1998).

3. Data and methods

We used teleseismic data recorded between January 2006 and May 2008 at 38 broadband seismic stations belonging to the North Anatolian Fault (NAF) passive seismic experiment ([dataset]Beck and Zandt, 2005; Biryol et al., 2010). For each station, we selected the events with high signal-to-noise ratio (SNR) waveforms using a visual inspection process. These waveforms were extracted from a list of about 1000 teleseismic events with magnitude ≥ 5.5 that occurred at epicentral distances (Δ) between 30° and 100°. Most of the events come from the first quadrant for the selected Δ range, where the major seismogenic zones are located. Nonetheless, a good azimuthal coverage is achieved for almost all stations. An example of such coverage is shown in Fig. 3 for station DOGL. The selected three-component seismograms are then rotated into the ZRT reference system, where R is the Radial direction along the great circle path from the epicenter to the station, T is the Transverse direction perpendicular to R in the horizontal plane, and Z is the vertical component. In RF analysis, the Z component of the

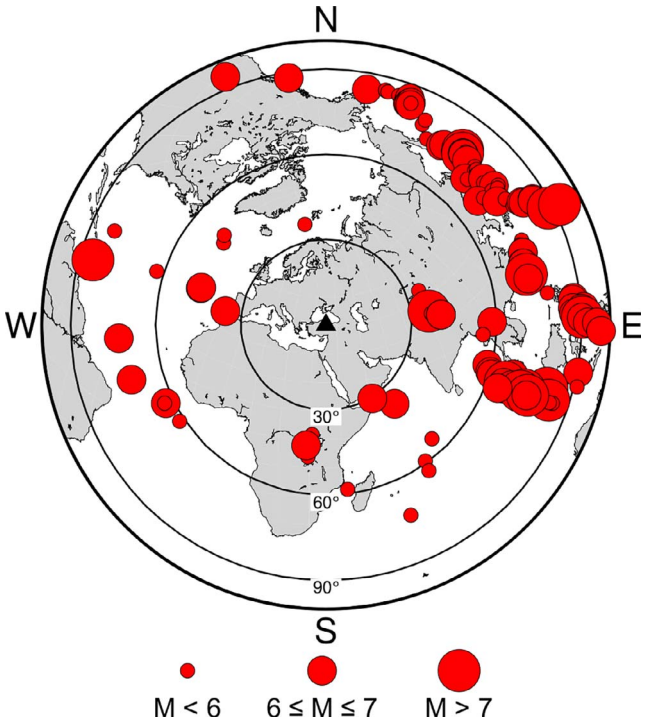

Fig. 3. Azimuthal equidistant projection centered at station DOGL with the source location of the teleseismic events used to compute the RF dataset for this station (black triangle). Only events from 30° to 100° of epicentral distance have been used. Size of circles is proportional to event magnitude (M) as per legend.

observed seismograms is taken as a proxy of the source wavelet, while horizontal components hold information about the near receiver S-wave velocity structure. The latter can be recovered after deconvolution of the vertical component from the horizontal ones. In this work, RFs are computed through the frequency domain deconvolution method developed by Di Bona (1998).

A Gaussian filter with low-pass frequency of ~1 Hz (Gaussian filter width a = 2) is applied to each RF, in order to rule out the effect of high-frequency noise. This choice limits the vertical resolution of the RFs to about 2–4 km (Piana Agostinetti and Malinverno, 2017). Both radial receiver function (RRF) and transverse receiver function (TRF) are computed from the three-component seismograms of a single event. After RFs are obtained, another visual inspection is performed, and only RF with acceptable SNR, small "ringing" and small amplitudes for delay times < 0 s are retained. This produces a total number of ~7100 RFs with an average value of ~180 RFs per station.

In a flat-layered and isotropic medium, only P-to-SV conversions are generated and no energy should be observed on the TRF (Savage, 1998). However, the presence of anisotropy and/or dipping velocity contrasts at depth (called 3-D features hereinafter) rotates the energy out of the source-receiver plane and produces P-to-SH conversions that are commonly observed on the TRF (Park and Levin, 2016). In this case, two-lobed (360°) or four-lobed (180°) periodicity in amplitudes and delay times as a function of back-azimuth (ϕ) are expected on both TRF and RRF (Levin and Park, 1998; Audet, 2015; Bianchi et al., 2015).

In order to assess the quality of the final RF dataset and to have a first glimpse at the contribution of 3-D features beneath each station, we plot both the RRF and TRF as a function of ϕ, after stacking in ϕ and Δ with bins of 20° and 40° width respectively, and 50% overlap to increase the SNR. In Fig. 4 we show two examples for stations ALIC and DOGL, which are located on top of the surface trace of two major active faults of the area, i.e. the NAF and the ESF, respectively. Although the final back-azimuthal sweeps are different between these stations, both of them show azimuthal variations in amplitude and delay times of the conversions along the RRF and TRF components. In this work, blue (red) color is used for positive (negative) pulses associated with an increase (decrease) of velocity with depth. On the RRF sweeps, the strong positive pulse at about 5.5 s can be associated with the conversion originated at the Moho. In the time window preceding the Moho arrival, crustal complexities beneath both stations are represented by high-amplitude pulses (both positive and negative). High amplitudes are also observed on the TRF panels at both stations for delay times between 0 and 6 s. This observation indicates that strong P-SH conversions take place at crustal depths. Moreover, clear patterns and periodicity can be observed in the waveforms on the TRF panels suggesting the presence of 3-D features at depth. In such complex tectonic settings, useful information about the subsurface can be extracted from both RRF and TRF.

In the next section, a simple, yet effective method is presented for the analysis of both the "isotropic" and "anisotropic" components of the RF dataset, i.e. the energy contained in the RF dataset generated from bulk S-wave velocity discontinuities, also referred as "isotropic structure", and from anisotropic materials at depth, also referred as "anisotropic structure".

3.1. Harmonic decomposition

Classical RF studies assume isotropic and flat-layered media for which the response of the subsurface is invariant with the back-azimuth, resulting in all the P-to-S converted energy to be confined in the RRF. Anisotropy and/or dipping velocity contrasts introduce amplitude and delay time variations as a function of back-azimuth on both RRF and TRF with distinct periodicity (either π or 2π). These effects are coupled on the RRF and TRF, drastically increasing the complexity of a given RF dataset. This makes even a qualitative analysis of raw RF datasets (as those shown in Fig. 4) difficult, leading to strongly non-unique interpretations. To overcome this difficulty, RRF and TRF should be analysed jointly. The harmonic decomposition technique provides a simple way for the simultaneous analysis of the RRF and TRF (Bianchi et al., 2010; Audet, 2015). This technique aims at separating

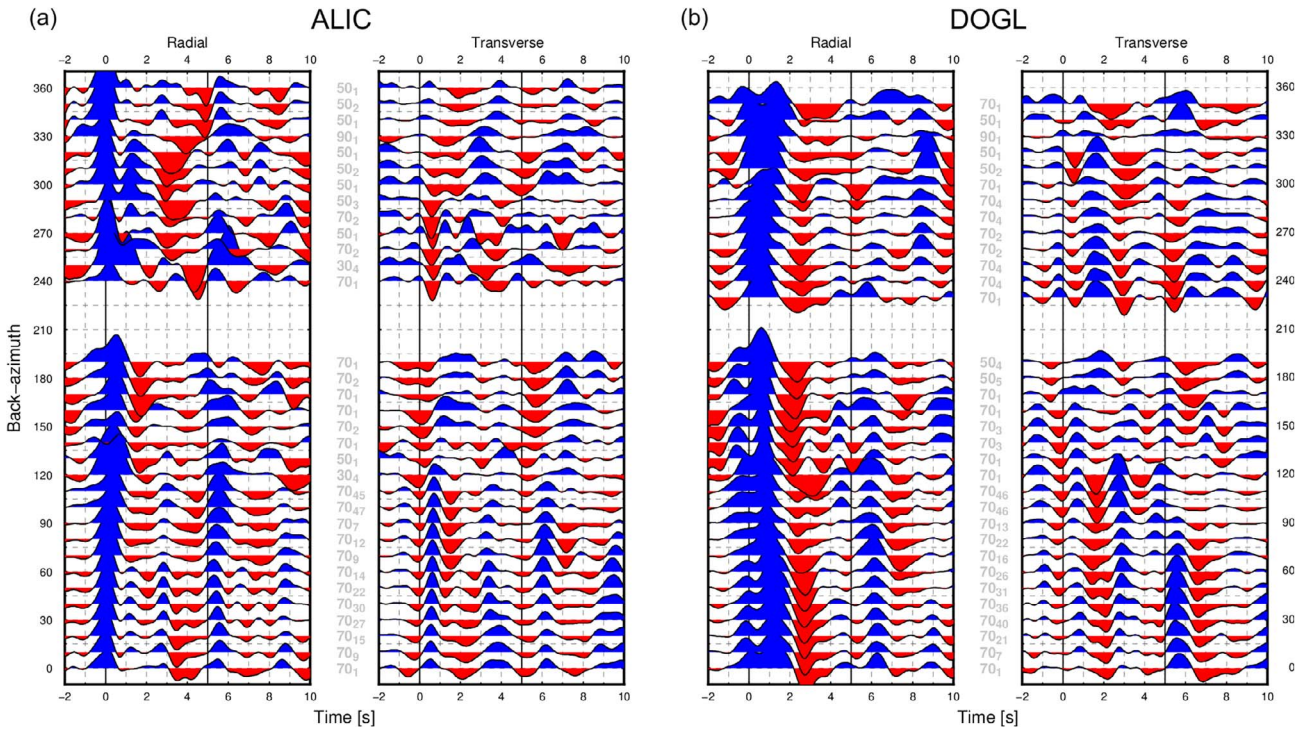

Fig. 4. Binned Radial and Transverse RFs for stations (a) ALIC and (b) DOGL, plotted as a function of back-azimuth. Gray numbers indicate the central epicentral distance used in the binning procedure. Small numbers indicate the total number of RFs making up each individual bin. Blue (red) pulses correspond to an interface with a positive (negative) downward velocity jump. (For interpretation of the references to colour in this figure legend, the reader is referred to the web version of this article.)

the isotropic response from the response induced by 3-D features at depth exploiting the azimuth-dependent signatures produced by the latter. This represents a clear advantage over classical RF analysis, as the RF dataset is partitioned into azimuth-invariant and azimuth-dependent components, thus facilitating subsequent interpretations.

More in detail, the method is based on the assumption that any RF dataset can be approximated as a series of cos[kϕ(t)] and sin[kϕ(t)], with k = 0, 1, 2, … In this way, the azimuth-dependent features can be isolated from the azimuth-invariant components. The k = 0 component is the constant azimuth term and describes the isotropic structure (i.e. contrasts in VS). At the core of the method is that the SNR of the two-lobed or four-lobed periodicity is enhanced on the k = 1 and k = 2 harmonics, respectively, by stacking the RRF and TRF with a positive shift in back-azimuth (+π/2k), as shown by Shiomi and Park (2008). The two-lobed periodicity (k = 1) is associated with the presence of dipping velocity contrasts or hexagonal anisotropy with plunging symmetry axis at depth. On the other hand, the four-lobed periodicity (k = 2) is uniquely produced by anisotropy with horizontal symmetry axis (Girardin and Farra, 1998).

Following Bianchi et al. (2010) and Liu et al. (2015), for each time step we can recover five coefficients, A(t), B(t), C(t), D(t), E(t), by solving the following linear system of equations for each time-step t in the RF dataset:

$$\begin{bmatrix} R_1(t) \\ \cdots \\ R_N(t) \\ T_1(t) \\ \cdots \\ T_N(t) \end{bmatrix} = \begin{bmatrix} 1 & \cos(\phi_1) & \sin(\phi_1) & \cos(2\phi_1) & \sin(2\phi_1) \\ \cdots & & & & \\ 1 & \cos(\phi_N) & \sin(\phi_N) & \cos(2\phi_N) & \sin2(\phi_N) \\ 0 & \cos(\phi_1 + \pi/2) & \sin(\phi_1 + \pi/2) & \cos(2(\phi_1 + \pi/4)) & \sin(2(\phi_1 + \pi/4)) \\ \cdots & & & & \\ 0 & \cos(\phi_N + \pi/2) & \sin(\phi_N + \pi/2) & \cos(2(\phi_N + \pi/4)) & \sin(2(\phi_N + \pi/4)) \end{bmatrix} \begin{bmatrix} A(t) \\ B(t) \\ C(t) \\ D(t) \\ E(t) \end{bmatrix}, \quad (1)$$

where N is the total number of events considered at each station. A(t) corresponds to the k = 0 harmonic, B(t) and D(t) are the cos[kϕ(t)] components and C(t) and E(t) are the sin[kϕ(t)] components of the k = 1 and k = 2 harmonics. With this configuration, cos[kϕ(t)] and sin[kϕ(t)] for k = 1 are orthogonal and oriented N-S and E-W, respectively. The same linear system can be solved using a negative phase shift (−π/2k), in which the effect of dipping structures and anisotropy is suppressed (Liu et al., 2015). In this case, the retrieved coefficients quantify the effect of complex 3-D structures, scattering, or incomplete geometrical coverage ("unmodeled" components hereinafter). The "unmodeled" coefficients can be seen as an estimate of the error associated with the harmonic decomposition. For further details on the method, the reader is referred to Park and Levin (2016).

The harmonic decomposition is applied to the RF dataset at each station, after stacking in ϕ and Δ with bin-width of 10° and 20° respectively, and with no overlap. This choice prevents the use of the same RF twice in the analysis, thus reducing any possible bias introduced by smoothing. As an example, we show the harmonic decomposition of the RF datasets at stations ALIC and DOGL in Fig. 5. The values of ϕ and Δ of each bin used to compute the harmonics are indicated with red stars for each station.

The two stations show different isotropic responses on the k = 0 plot. The P-to-S conversion originated at the Moho can be identified as the positive pulses at about 5.5 and 6.0 s on ALIC and DOGL, respectively. At earlier delay times, ALIC shows positive pulses at about 1 and 2.4 s while a broad negative pulse can be observed at 4 s. On the contrary, the pulse with highest amplitude at station DOGL is found at about 0.8 s, indicating the presence of a strong and shallow impedance contrast, followed by a negative pulse at 2.3 s.

The k = 1 harmonics (cos(ϕ) and sin(ϕ) traces) show higher amplitudes on the "modeled" part than on the "unmodeled", thus indicating a significant and coherent contribution from the azimuthally-varying structure beneath the two stations. Higher amplitudes are found in the first 6 s for both stations, suggesting a crustal origin of this signal. Both stations display a series of pulses with opposite polarities (derivative pulses) on both k = 1 components in the first 4 s, although station DOGL is dominated by the derivative pulse on the cos(ϕ) component with peaks at 1.6 and 3 s. Small amplitudes are observed on the k = 2 harmonics compared to k = 1. In addition, for the k = 2 harmonics, comparable amplitudes are observed between the "modeled" and "unmodeled" terms. These observations hold for the majority of the stations, thus, in the following, we exclude the k = 2 harmonics and restrict the analysis only to the first two order harmonics. We display the components of cos(ϕ) (oriented N-S) and sin(ϕ) (oriented E-W) separately for k = 1, giving a total of three harmonic coefficients (i.e. three time series).

3.2. Energy and map-orientation of 3-D features

The main aim of this work is to map the position of anisotropic bodies and/or dipping velocity contrasts at crustal depths and to determine their orientations. Based on the harmonics dataset previously described, we first perform a time-to-depth conversion of the k = 0 and k = 1 harmonics at each station. The standard IASP91 velocity model (Kennett and Engdahl, 1991) is used for this purpose. We use the mean slowness value at each station to perform the depth conversion. In principle, this choice could produce defocused results in the harmonics, if the range of slowness considered is broad. In order to estimate the error associated with this choice, we compare our results with an alternative approach in which the harmonic decomposition is performed in depth domain after time-to-depth conversion of the RF dataset (Audet 2015; Cossette et al., 2016; Tarayoun et al., 2017), thus preserving the information about slowness. The comparison points out

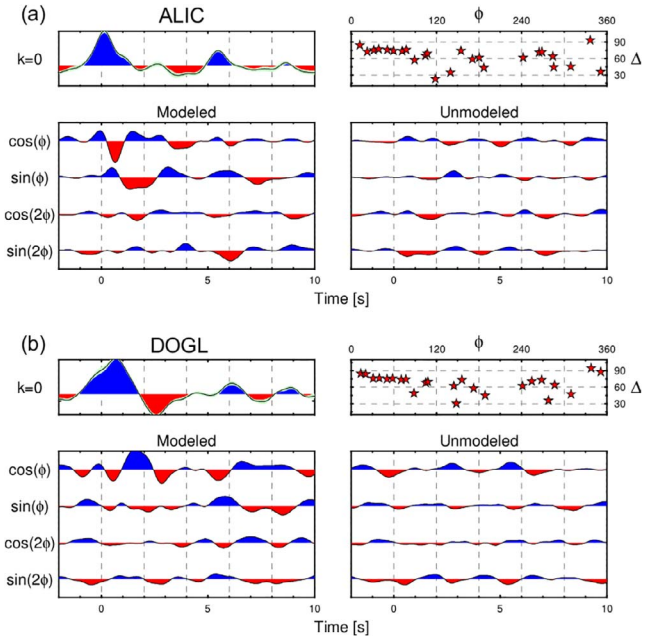

Fig. 5. Harmonic decomposition of RFs for stations (a) ALIC and (b) DOGL. k = 0 trace corresponds to the "constant", zero-order harmonic. cos[kϕ(t)] and sin[kϕ(t)] harmonics for k = 1, 2 are shown in the bottom panels for modeled (+π/2k shift in the stack) and unmodeled (−π/2k shift in the stack) parts. See text for details. Top right panel shows the geometrical distribution (in back-azimuth, ϕ and epicentral distance, Δ) of RFs used for the harmonic decomposition. The same amplitude scale is used in all plots.

that, given the distribution of events for the NAF experiment, small errors are produced by using the mean ray parameter and this effect is negligible in the crust (see Appendix A).

Considering that the inter-station distance is generally greater than 30 km, we build depth-profiles by juxtaposing single-station data and focus our attention on vertical and lateral variations of crustal structure (k = 0 harmonics) and position of 3-D features (from k = 1 harmonics) along the profiles.

As a proxy for the position of 3-D features at depth, we compute the sum of the squares of the (depth converted) "modeled" cos(ϕ) and sin (ϕ) terms for the k = 1 harmonics (Piana Agostinetti and Miller, 2014) and subtract the contribution of the "unmodeled" counterpart according to:

$$E(z) = [B(z)_M^2 + C(z)_M^2] - [B(z)_U^2 + C(z)_U^2] \quad (2)$$

where the subscripts M and U refers to the "modeled" and "unmodeled" harmonic coefficients and z is the depth axis. The resulting quantity E(z) (referred as "energy" hereinafter) highlights the position of 3-D features at depth in an intuitive way, thus making the interpretation of the results simpler. High energy at a certain depth may suggests the presence of either a contrast in anisotropic properties (top or bottom of an anisotropic body with plunging symmetry axis) or a dipping velocity contrast.

In addition, the map-projected orientation of 3-D features can be retrieved from the depth-converted k = 1 harmonics. In fact, from the particle motion of the cos(ϕ) (N-S component) and sin(ϕ) terms (E-W component) it is possible to infer the trend of the unique symmetry axis of hexagonal anisotropy (or the dipping direction of a dipping velocity contrast) responsible for the observed signal (Bianchi et al., 2010). In a simple linear regression of the particle motion at each station, the orientation of 3-D features is recovered from the slope parameter. In principle, we could estimate a value of the slope parameter at each depth point; however, as in Audet (2015), we found more stable results if a range of depths is considered. An example of the particle motion for the 0–15 km depth range at station ALIC is shown in Fig. 6. We estimate the trend direction (green arrow) from the slope parameter, together with its uncertainties (gray arrows), for each station, finding errors of usually less than 15° (95% confidence interval).

The retrieved orientation (green arrow) can have multiple interpretations. It could, for example, represent the trend of the plunging symmetry axis of hexagonal anisotropy. In this case, the axis would plunge towards either NW or SE. Some ambiguities arise in this case, as no information about the nature of the symmetry axis (fast or slow) is available (see Sherrington et al., 2004 for details). A second possible interpretation provides the dipping direction of a dipping velocity contrast striking NE-SW. This ambiguity is stronger in the upper crust, but it diminishes with increasing depth, where strongly dipping velocity jumps (more than 30°) are less likely to occur, and hence anisotropy is assumed as the main cause of the observed signals.

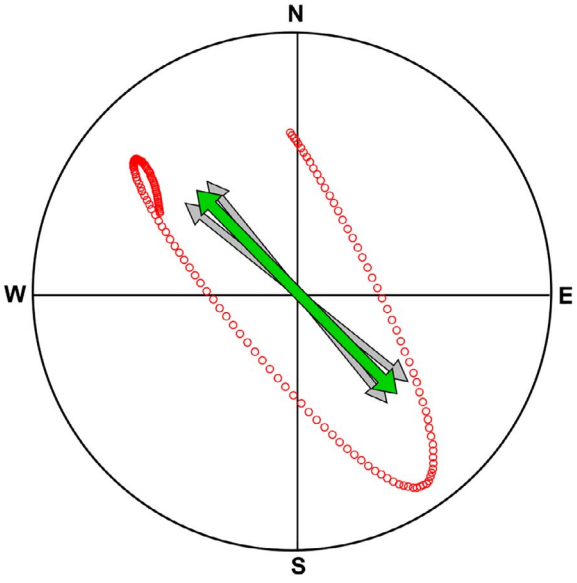

Fig. 6. Particle motion for the 0–15 km depth range at station ALIC. Particle motion (red points) of the N-S and E-W component of the first order harmonic. Trend of the symmetry axis (green arrow) is estimated through linear regression of the particle motion. Grey arrows indicate three standard deviations of the estimated slope parameter from the linear fit. (For interpretation of the references to colour in this figure legend, the reader is referred to the web version of this article.)

In the next section, to facilitate our interpretation, we follow Schulte-Pelkum and Mahan (2014b) and plot the direction normal to the retrieved trend direction (i.e. the strike). Therefore, for a dipping velocity contrast our map-projected strike can be directly interpreted as the strike of the dipping velocity contrast. On the other hand, for hexagonal anisotropy, this gives us the map-projected orientation of the plane perpendicular to the plunging symmetry axis. In case of negative anisotropy (unique slow symmetry axis), this is the strike of the fast plane, which can be interpreted as the strike of foliation or the strike of the plane of preferred cracks or mineral alignment. By plotting the map-projected strike together with the energy in a given depth range, we build energy maps with orientation of the 3-D features as seen by the RF data. This provides us with spatial information about the azimuthally varying structure and their first-order depth dependence.

4. Results and discussion

We apply the harmonic decomposition technique to all the stations in the area, and plot the results side by side along seven profiles (Fig. 7). In each panel of Fig. 7, we plot the topography of each profile with the location of the main active faults (NAF and ESF) together with the results of the harmonic analysis. For each station, the waveforms of the resulting harmonics are plotted individually. Blue lines are used to highlight our observations on the constant component. In the last plot of each panel, the energy associated with the k = 1 harmonics is displayed in grayscale. Here, green and orange boxes indicate areas of strong energy at depths smaller and greater than 30 km. Location of the profiles is shown in Fig. 2. Five profiles (from AA′ to EE′) follow S-N direction and cross the main active faults in the area (NAF and ESF). The last two profiles, FF' and GG', run W-E and are designed to investigate the crustal setting of the northern and southern blocks divided by the NAFZ. Lateral variations in both k = 0 and k = 1 harmonics are evident in the majority of the profiles.

4.1. Crustal structure and Moho topography

It is beyond the scope of this paper to discuss in detail the isotropic structure of the area, as the focus is mainly on 3-D features. Given that the inter-station distance does not allow for overlapping zones of sensitivity in the crust, our observations are therefore generally limited to a single-station approach. With a vertical resolution of 2–4 km, k = 0 harmonics at the stations analysed in this study indicate that the Moho topography is generally a continuous feature at about 40 km (Fig. 7). This result is in good agreement with earlier crustal thickness estimates from RFs in the same area, which reported fairly consistent values with the present study, i.e. ~35–40 km (Özacar et al., 2010; Vanacore et al., 2013). Nevertheless, our results show a few local examples where the identification of the Moho is difficult or ambiguous. Along profile CC′ (Fig. 7c) for example, a positive pulse is located at about 40 km depth for almost all stations. However, the continuity of the Moho Ps phase is broken at two neighbouring stations (CAYA and PANC) between 75 and 105 km along the profile. Station CAYA shows almost no signal between 25 and 50 km depth. The following station to the north, PANC, possesses a positive pulse at about 30 km, which is quite shallower than the general Moho depth along this profile. These two contiguous stations are located between the ESF to the south and the IAESZ to the north. In

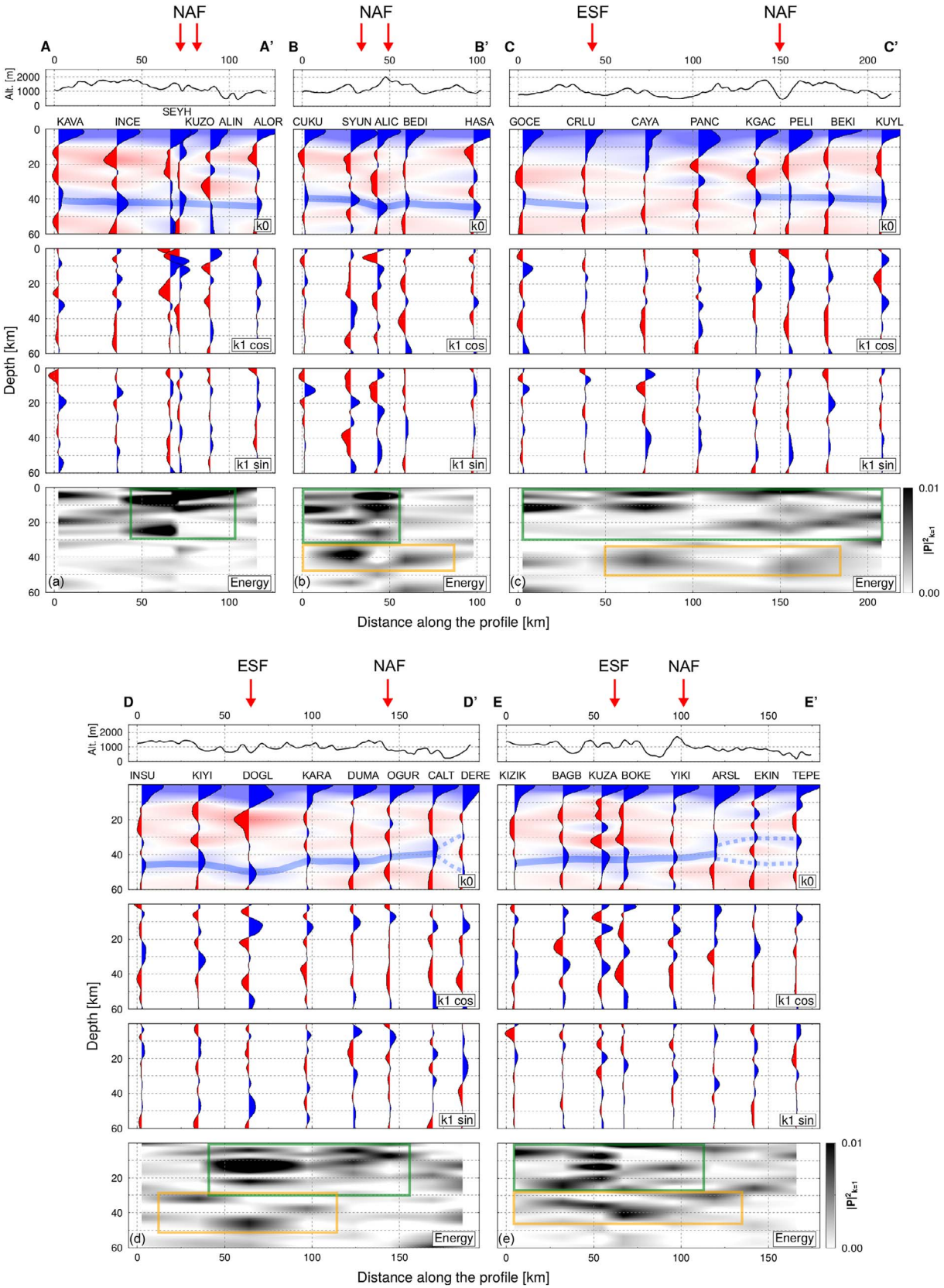

Fig. 7. Harmonic decomposition results. Time-to-depth converted harmonics are shown along seven profiles. The surface trace of each profile is indicated in Fig. 2. For each profile, the top panel indicates the surface topography for reference. The following three panels display the k = 0 harmonic, and the cos[kϕ(t)] and sin[kϕ(t)] components of the k = 1 harmonic. Wiggles are plotted on top of an interpolated image for clarity. The bottom panel shows the energy calculated from the k = 1 harmonics, as explained in the main text. Red arrows indicate the position of the surface traces of the North Anatolian Fault (NAF) and the Ezinepazari-Sungurlu Fault (ESF). The same scale is used for harmonics and energy amplitudes between different panels.

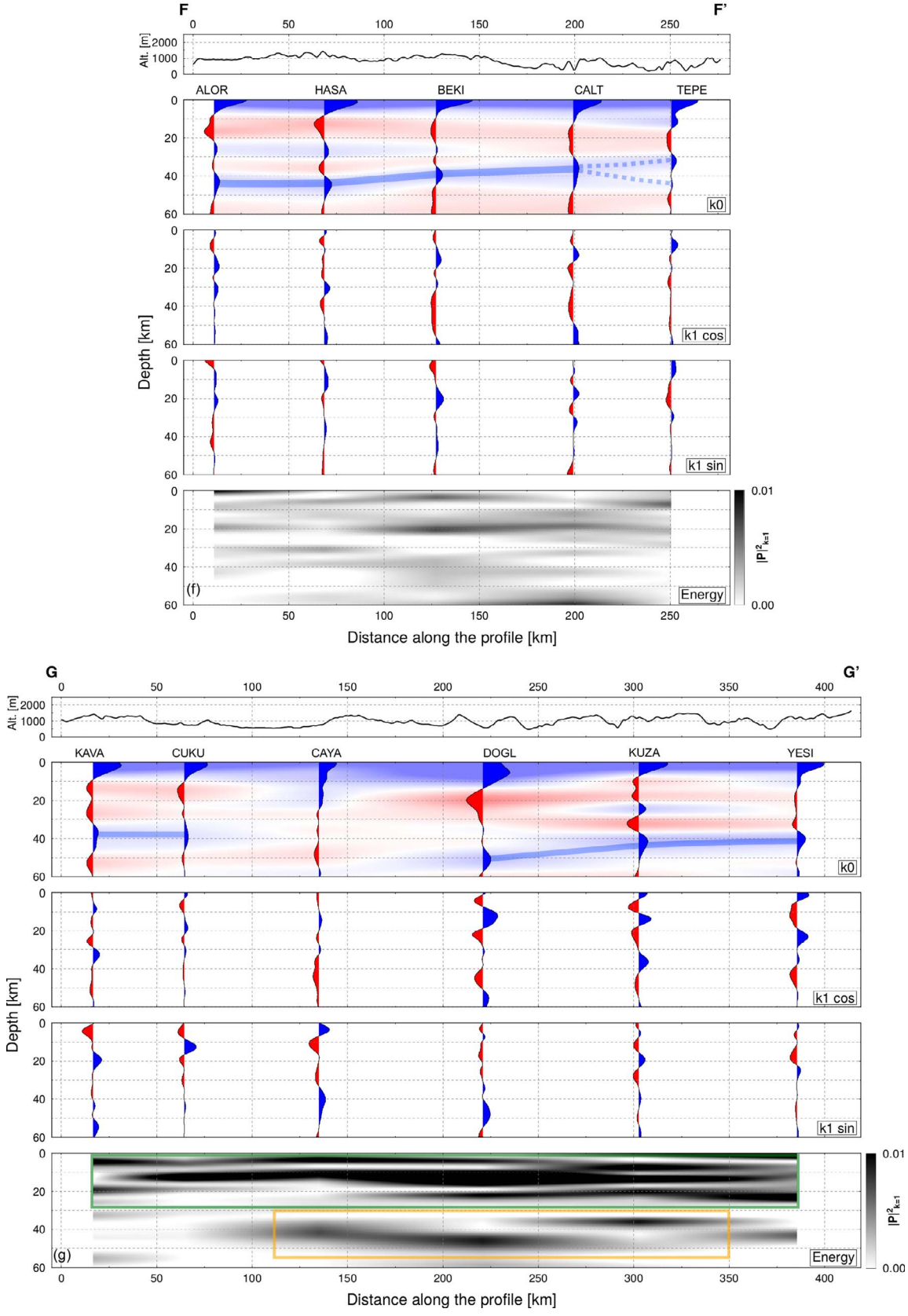

Fig. 7. (*continued*)

addition, the k = 0 harmonic at station PANC shows the highest energy at about 5 km depth, and very broad direct P-wave pulses are observed in the first 110 km of the profile. Stations CAYA and PANC are located within the Kırşehir Massif tectonic unit. Here, the presence of the Çankırı Basin and its sedimentary infill is likely responsible for producing reverberations in the sedimentary pile that can interfere with the primary Ps conversion from the Moho, thus producing the observed broad direct P-wave pulse.

The main structural differences between the crust of the blocks located south and north of the NAFZ are evident when comparing the two longitudinal profiles FF′ and GG′ shown in Fig. 7g and f, respectively. In FF′, the Moho Ps pulse is continuous along the length of the profile, although it tends to get shallower and broader towards the east. In GG′, the pulse related to the Moho is located at a depth of about 40 km, except for station CAYA, which does not show a clear Moho signal, and for station DOGL, which has a deeper Moho (50 km depth). At the same time, along GG′, no continuity of intra-crustal signals can be observed, indicating a more heterogeneous setting in the crust. The intense deformation history that affected the southern block, together with its tectonic activity, result in a more heterogeneous crust, in accordance with 3-D local earthquake tomography (Yolsal-Çevikbilen et al., 2012). This dramatically increases the complexity of the RF waveforms with respect to the more geologically stable northern block.

Finally, there is no clear evidence of Moho offset related to the NAFZ, which confirms previous lower frequency observations from S-RF (Kind et al., 2015). However, the NAFZ clearly affects intra-crustal structures in the first 20 km (see Fig. 7. profiles AA′, EE'). A smaller inter-station distance would be required in order to study the lateral continuity of intra-crustal Ps conversions across this major fault system.

4.2. Seismic anisotropy

In the profiles shown in Fig. 7, high values of the energy associated with the k = 1 harmonics indicate a widespread contribution from 3-D features throughout the crust of the study area. Two main observations can be drawn from these results. First, a substantial energy drop from south to north of the NAFZ is observed along profiles BB′, DD′ and EE′. In addition, highest energy with complex patterns is located in between active faults where crustal structure is also complex (profiles AA′, CC′ and DD′ of Fig. 7) and, at least locally, the NAF controls the transition of the energy from south to north (profile BB′ in Fig. 7). Second, the main source of the energy signal is located within the upper and middle crust, where the highest amplitudes are observed. Deeper (greater than 30 km depth) sources of the observed energy show lowest amplitudes and less continuity. Finally, strong differences in terms of energy are observed between profiles FF′ and GG′, both oriented W-E, and located respectively in the northern and southern blocks divided by the NAF. GG' shows much stronger energy than FF′ throughout the crust.

We complement the depth-dependent information about 3-D features shown in Fig. 7 with a spatial mapping analysis on three discrete depth ranges: 0–15, 15–30 and 30–60 km, roughly corresponding to the upper crust, middle crust and lower crust plus upper mantle. For each of these depth ranges, we build interpolated energy maps for the k = 1 harmonics by summing the contribution of each point in a given depth range. At the same time, we calculate the direction of the 3-D features, as explained in the previous section, from the slope parameter of the linear regression of the particle motion in the same depth range. The results are shown in Fig. 8 and summarized in Table S1 of the supplementary material.

In the following, we discuss our results regarding the energy distribution, in terms of depth-dependent and spatial features.

4.2.1. Upper crust

The strongest azimuthally varying signal is generated in the first 15 km of the crust. Overall, the energy observed in this depth range is higher than that originated in the deeper portion of the crust and upper mantle (compare the total energy in Fig. 8 at different depths). Between 0 and 15 km depth (Fig. 8a), two spatial zones with distinctive characteristics are separated by the NAFZ, confirming what was already observed along the profiles of Fig. 7. Stations located north of the NAF show consistently low energy in the k = 1 harmonics. Conversely, on top of the NAF and southwards, higher energy is found for more than half of the stations (15 out of 28 stations). In this region, in addition, the pattern is more heterogeneous, with alternating low and high

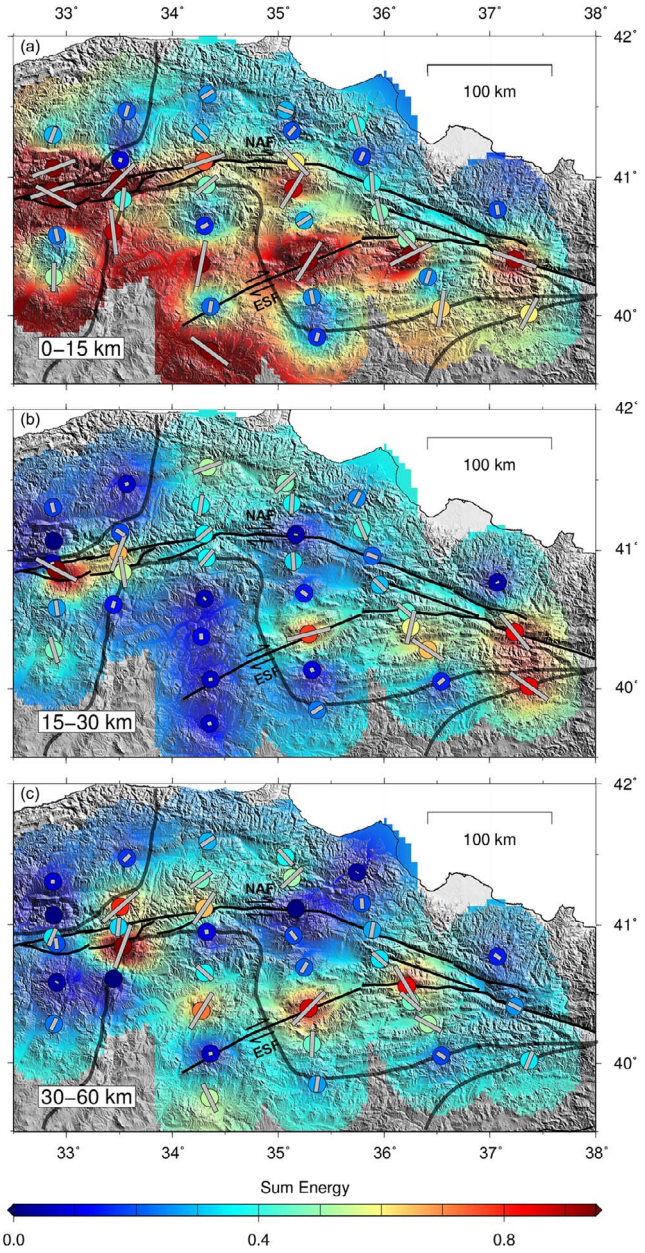

Fig. 8. Maps of the total energy at three different depth ranges. (a) 0–15 km, (b) 15–30 km and (c) 30–60 km depth. The colorscale indicates the sum of the energy on the k = 1 harmonics in the corresponding depth range. Strike of the plane normal to the axis of symmetry is indicated with a gray bar at each station and scaled by the total energy in the same depth range. The major tectonic features in the area are drawn with black lines (see also Fig. 2).

energy values, thus giving rise to a higher spatial frequency variation when compared to north of the NAF. A second order observation indicates that almost all stations (13 out of 15 stations) with high energy (greater than 0.5) are located on top or in close proximity of active faults (NAF and ESF) or ancient suture zones.

This is perhaps the most striking feature of our results: the spatial distribution of the energy associated with the k = 1 harmonics in the upper crust is clearly influenced by the structural setting of the area. In particular, we identify the well defined partitioning between low-energy stations north of the NAF and high-energy stations on top of the NAF and southwards (Figs. 7 and 8).

In our RF analysis, both dipping velocity jumps and seismic anisotropy contribute to the observed energy, especially in the upper crust, where the contribution of dipping layers can be strong. In our simple approach, the discrimination between the two effects is not easy and even an inversion approach would produce non-unique results. A direct

interpretation of our results in the upper crust is further complicated by the possible presence of reverberations induced by shallow low-velocity layers, as those present in sedimentary basins with complex geometries (see Appendix B).

Despite the inherent non-uniqueness of our results, shear wave splitting analyses performed on local seismicity across the different portions of the NAFZ yielded a signal with a maximum ~0.2–0.3 s of time delay, which has been attributed to the presence of anisotropy within the first 8–10 km of the upper crust (e.g., Peng and Ben-Zion, 2004; Hurd and Bohnhoff, 2012; Eken et al., 2013). In addition, a recent 3-D radially anisotropic tomography (Çubuk-Sabuncu et al., 2017) has shown the presence of strong (20%) negative anisotropy throughout the Anatolian crust at a regional scale. For these reasons, we will discuss the possible implications of our results in terms of anisotropy only.

If we assume slow anisotropy in the upper crust, our results (Fig. 8a) indicate the strike of the fast plane perpendicular to it, corresponding to the strike of bedding, foliation or alignment of cracks or macroscopic fractures. Under this perspective, our retrieved strikes for high-energy stations located on top of the main active faults of the area (NAF and ESF) match the orientations of the faults within the errors. Fault parallel strike for these stations is in good accordance with previous shear wave splitting studies in different portions of the NAFZ (Li et al., 2014) and with RFs studies along the San Andreas Fault (Porter et al., 2011; Audet, 2015). The direction of SH_{max} in the study area was estimated from local seismicity (Karasözen et al., 2014). It shows an average NW-SE orientation, thus being very different from our retrieved strikes of the fast plane assuming slow anisotropy. Therefore, our results support a structure-induced origin of the observed anisotropy rather than a stress-driven mechanism. This agrees with the findings of Li et al. (2014). In any case, the inter-station distance in the present study does not allow for an estimate of the width of the damage zone, which however affects only the stations located on top of active faults (Fig. 8a). This is in accordance with Li et al. (2014), where the width of the damage zone around the Karadere–Düzce branch of the NAFZ was estimated to be around 3 km, as well as with Audet (2015), who reported similar estimates around the San Andreas Fault.

Although our approach does not allow to retrieve the full orientation of the symmetry axis in 3-D, our results imply a dominant contribution from anisotropy with dipping symmetry axis, revealed from the analysis of the k = 1 harmonics. This observation suggests a strong similarity between the deformation regime around the NAFZ and the San Andreas Fault, where the anisotropic inversion of RF data showed a substantial dip (about 45°) of the slow symmetry axis of anisotropy in the close proximity of the main fault (Audet, 2015).

Both the k = 0 and k = 1 harmonics in Fig. 7 and the spatial distribution of energy in the upper crust in Fig. 8 suggest an asymmetric distribution of elastic properties across the NAFZ. This confirms what discussed in detail by Şengör et al. (2005) and Le Pichon et al. (2005). In particular, the presence of a bimaterial interface developed as a result of the cumulative production of rock damage associated with the faulting process (Ben-Zion and Sammis, 2003 and references therein) was reported in several studies (e.g. Bulut et al. 2012; Ozakin et al., 2012; Najdahmadi et al., 2016), along different segments of the NAFZ. Our results corroborate this hypothesis in the study area.

4.2.2. Middle crust

Between 15 and 30 km depth (Fig. 8b), the intensity of anisotropy diminishes for some of the near-fault stations, suggesting a progressive closure of fractures due to increasing confining stress, as observed also on a more eastern portion of the NAF from shear wave splitting measurements (Li et al., 2014). However, a few near-fault stations located on the westernmost part of the study area (in correspondence of the NAF) and in the central part of the ESF show a considerable amount of energy. This may suggest a differential closure of fractures around the faults, implying a depth extent of the damage zone below 15 km (see depth profiles AA′, BB′ and DD′) for some stations.

High-energy stations located on top or in close proximity of ancient suture zones (IPS, IAESZ, and ITS) are more difficult to interpret, as they show both parallel (ALIN and CUKU) and oblique (KIZIK and CAKM) strikes.

Away from active faults, anisotropy is generally lower, but some local high-energy anomalies are observed at different depth ranges, south of the NAF. We suggest that some of these spots of high anisotropy are correlated with the presence of the uplifted blocks of accreted and strongly deformed basement recognized by Yolsal-Çevikbilen et al. (2012), above 30 km depth in the central and eastern part of the study area (south of the NAF). Alternatively, the localization of intense deformation which has been taking place south of the NAF may be considered responsible for the observed seismic anisotropy at mid-crustal depths, as heavily fractured and fluid-saturated rocks, alignments of anisotropic minerals and crustal flow can produce directional velocity changes at different crustal depths (Fouch and Rondenay, 2006; Mainprice et al., 2007).

4.3. Lower crust and upper mantle

The interpretation of deep anisotropy (between 30 and 60 km, Fig. 8c) is difficult. The number of high-energy (energy > 0.5) stations is small (six) and their spatial distribution is scattered. Nevertheless, we notice that these stations are located close to the central-western part of the NAFZ, along the ESF, and that five of them display strikes oriented NE-SW. This agrees with the 3-D full-waveform tomography study of Çubuk-Sabuncu et al. (2017), which revealed deep negative radial anisotropy ($V_{SV} > V_{SH}$) in the close vicinity of known weakness zones, including the NAFZ, as well as with the orientation of the FDPs from SKS splitting in the same area (Biryol et al., 2010). Tentatively, we can also compare the results from this layer with the results obtained by Vinnik et al. (2016) from the analysis of the k = 2 components of P-RF, for the same array of stations used in this study. Using an array-averaged RF dataset for the harmonic decomposition, these authors reported intensity of horizontal-axis anisotropy between 3 and 5% (the highest value in their study) and fast direction between 30° and 60°, in a depth range between 35 and 60 km. Our results for high-energy stations at the same depth level are in good agreement, at least for the direction of anisotropy. Vinnik et al. (2016) argued that this sub-Moho anisotropy is likely frozen in the upper mantle . Our results support this idea.

5. Conclusions

In this paper we use teleseismic receiver functions to study the crustal structure and map crustal anisotropy around the central portion of the North Anatolian Fault Zone. We show that a simple yet effective harmonic decomposition of RFs can be used to reveal first-order features of the crust, as well as to locate the presence of anisotropy as a function of depth.

Our findings indicate strong asymmetry of crustal properties around the North Anatolian Fault. The southern block possesses a complex crustal structure and is highly anisotropic when compared to the simpler and more weakly anisotropic crustal block in the north.

The Moho is generally a continuous feature at around 40 km showing no major offsets across the area. On the other hand, the intracrustal structure is strongly affected by intense deformation in the southern block.

The anisotropic signal is strongest in the first 15 km of the crust and is predominantly located on top of the major active fault zones (NAFZ and ESF). Here, the strike of the fast plane of anisotropy is fault-parallel, implying a structure-induced mechanism as the dominant source for observed crustal anisotropy. Progressively increasing confining stress around the faults contributes to the general observed trend of decreasing anisotropy with depth.

At middle crustal depths (15–30 km), spots of high anisotropy in the southern block may have multiple interpretations. For stations close to

the faults, they could indicate that the extent of the damage zone at depth could go beyond 15 km. Away from the faults, alignment of minerals in uplifted basement blocks can be responsible for the observed anisotropic signal.

Between 30 and 60 km our results support the idea of an upper mantle layer with frozen-in anisotropy directed NE-SW, as suggested by previous studies in the same area.

Acknowledgement

We thank the editor Vernon Cormier, Pascal Audet and one anonymous reviewer for their valuable comments which helped to strongly improve the quality of this manuscript. Thanks are also due to Frederik Tilmann for his support and help in shaping the manuscript as well as interpreting our findings. We are grateful to the Incorporated Research Institutions for Seismology Data Management Center (IRIS-DMC) for making continuous broadband data open to the international scientific community. Data for the NAF experiment (doi: http://dx.doi.org/10.7914/SN/YL_2005) are available from the IRIS Data Management Center at http://www.iris.edu/hq/. This research has been conducted with the financial support of Science Foundation Ireland & the Marie-Curie Action COFUND under Grant Number 11/SIRG/E2174, and within the framework of the research grant (TÜBİTAK–CAYDAG-115Y248 Project) provided by the Scientific and Technological Research Council of Turkey (TÜBİTAK). TE and TT acknowledge financial support from the Alexander von Humboldt Foundation (AvH) towards computational and peripherals resources. N.P.A.'s research is funded by Austrian Science Foundation (FWF) under Grant Number M2218-N29. We also thank *TIDES: TIme-DEpendent Seismology action (ES1401),* within the framework of the *European Cooperation in Science and Technology* (*COST*), for providing financial support for A.L., T.E., and T.T to participate at *TIDES* Advanced Training School–Bertinoro (Italy) between June 1 and 5, 2015, where this study was planned to be initiated.

Appendix A

In this work, the harmonic decomposition of the RF dataset at each station is performed in time domain. The resulting harmonics are subsequently converted to depth using the mean ray parameter of the whole dataset. A possible shortcoming of this approach is that, if the distribution of events spans over a broad range of epicentral distances, the resulting harmonics can be affected by incoherent angular stacking. This could prevent an optimal focusing of the waveforms and increase the uncertainties in the position of the pulses at depth.

Recent works (Audet 2015, Cossette et al., 2016, Tarayoun et al. 2017) have proposed a solution to this problem. The RF dataset is first converted to depth, in order to preserve the information about the ray parameter for each RF. Afterwards, the harmonic decomposition is performed in depth domain.

In this appendix, we compare the two methodologies for station BEKI. The results are shown in Fig. A1.

The harmonics (k = 0 and k = 1) computed as described in the main text are drawn in black, while those resulting from the depth-domain harmonic decomposition are in red. Very small differences in the resulting waveforms are observed. The major differences are below 30 km and encompass the depth range of the Moho pulse. We performed the same comparison for all the stations analysed in this study, finding similar results.

This allows us to estimate the error due to using a mean ray parameter for the whole dataset in our time-domain decomposition. For the k = 0 harmonic, the differences in amplitude between the two methods are smaller than the bootstrap uncertainties on the computed waveform (2σ, blue dashed line in Fig. A1a).

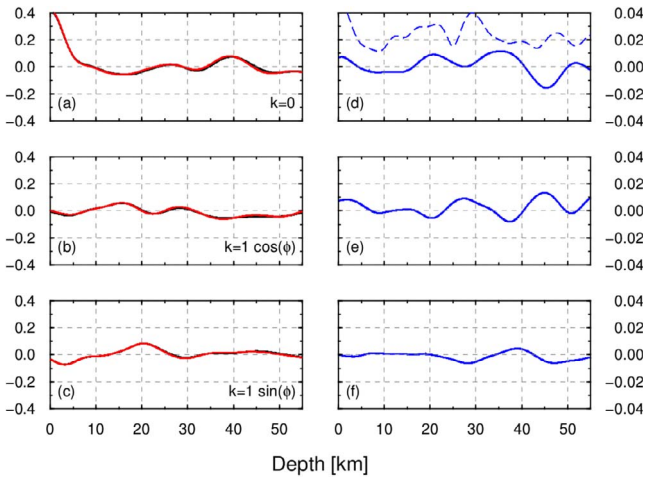

Fig. A1. Effect of averaging ray parameter values on harmonic decomposition. (a), (b), (c) Comparison between harmonics calculated as described in the main text, using a mean ray parameter value for the whole RF dataset (black curves), and harmonics calculated in depth domain after depth-conversion of individual RFs, performed with the corresponding ray parameters (red curves). (d), (e), (f) Difference between the red and black curves. Blue dashed line is 2σ uncertainty on k = 0 component retrieved with a bootstrap analyis. Note that the range of values of the vertical axis differs by an order of magnitude between the two columns.

Appendix B

In the upper crust, the presence of shallow low-velocity layers within sedimentary basins induces reverberations within the sedimentary pile, due to the strong impedance contrast at the sediment/basement interface. Depending on the elastic properties (density, seismic velocity, attenuation) and thickness of the sediments, these reverberations can strongly affect early portions of the RF waveforms after the primary arrival from the sediment/basement interface. This can, in principle, mask the signal from deeper (and possibly anisotropic) crustal structures.

Here, synthetics from a simple crustal model (Table A1) are used to investigate the effects of such reverberations on the observed azimuth-dependent signals.

In Fig. A2, we show that in the absence of dipping velocity contrasts, basinal reverberations affect the shape of the k = 0 harmonic. The primary

Table A1
Parameters of the synthetic model in Figs. A2 and A3. Note that in A3 the interface between Layers 1 and 2 dips N90°E of 15°.

Layer	Thickness (km)	Density (kg cm^{-3})	V_S (km/s)	V_P/V_S	Ani P/S (%)	Trend (deg)	Plunge (deg)
1	2.0	2.6	2.0	2.0	0	0	0
2	7.0	2.6	3.0	1.72	0	0	0
3	5.0	2.6	3.0	1.72	10	0	45
4	26.0	2.6	3.0	1.72	0	0	0
HS	–	3.3	4.4	1.80	0	0	0

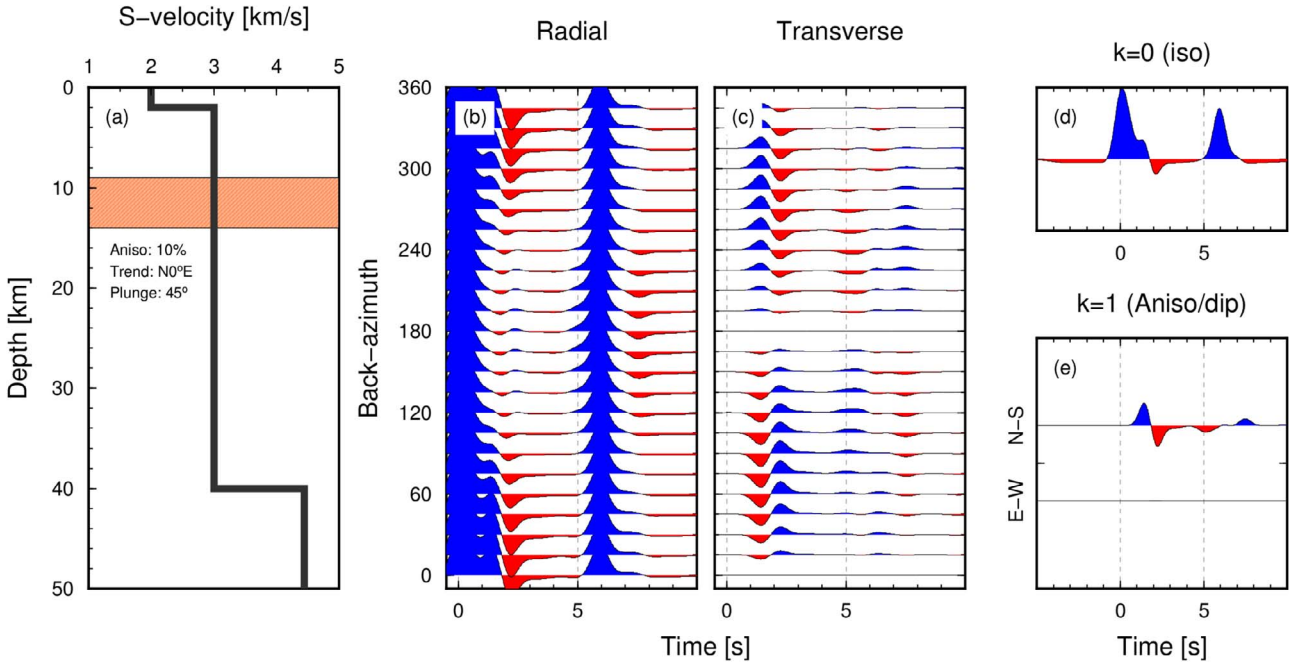

Fig. A2. Effect of shallow low-velocity layer on k = 0 and k = 1 harmonics. (a) Crustal S-wave velocity model used for the synthetic test. The anisotropic layer is identified by the orange box and described by its parameters (intensity of anisotropy, trend and plunge of the symmetry axis). (b) and (c) Radial and Transverse RFs homogeneously distributed with back-azimuth and fixed epicentral distance of 60°. (d) and (e) k = 0 and k = 1 harmonics computed from this synthetic RF dataset.

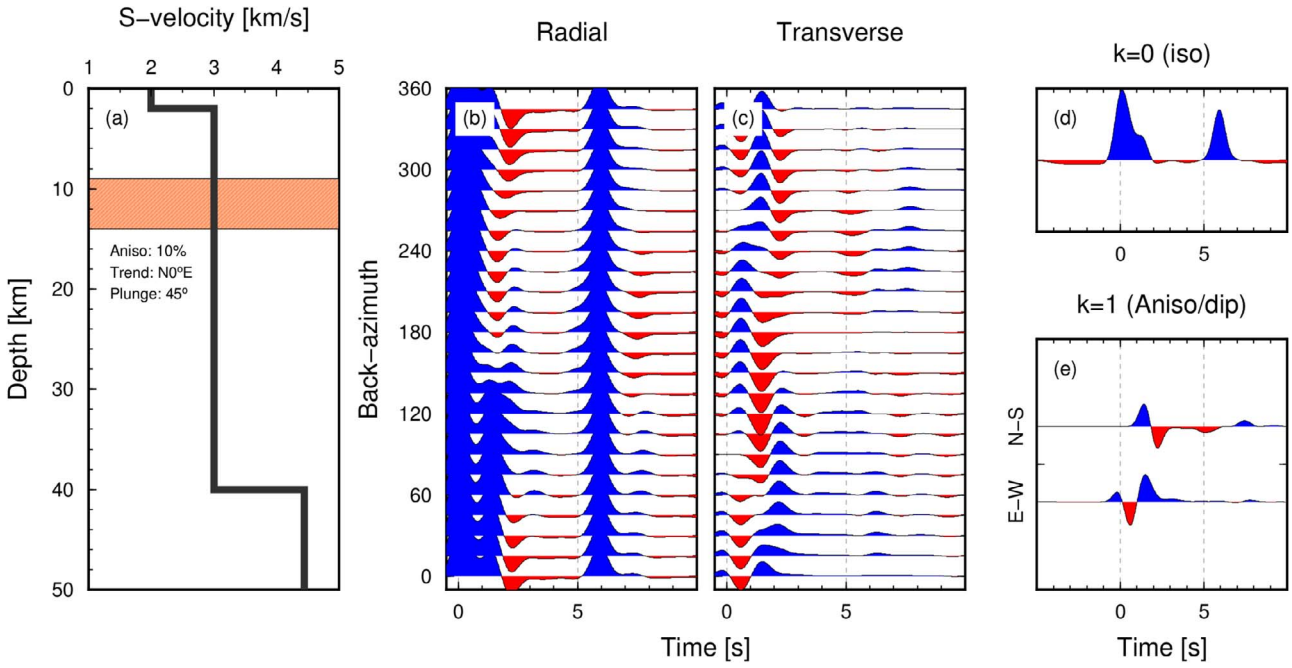

Fig. A3. Same as Fig. A2 but with the velocity contrast at 2.5 km depth dipping East by 15°.

converted phase from the bottom of the sediments is entirely within the direct P-wave pulse. Its multiples are seen at about 1.2 and 2 s. However, no effect induced by reverberations is seen on the k = 1 harmonics where the signature of the anisotropic layer between 9 and 14 km depth is clear on the N-S component.

On the other hand, in Fig. A3 a basement dipping N90°E is added to the model. In this case, reverberations of the phase associated with the dipping basement give rise to an azimuthally-varying signal that gets mapped as a positive pulse on the k = 1 harmonics (blue pulse on the E-W component at about 1.5 s).

With respect to primary conversions, multiple phases sample portions of the subsurface farther away from the station. Thus, for reverberations to be observed on real data, it is required that the source of the periodic signal in back-azimuth (either the anisotropic body or the dipping velocity contrast) is spatially continuous and has a lateral extension of at least twice its depth. In any case, Fig. A3 shows that complex geometries in the shallow crust can prevent a unique characterization of the anisotropic signal and care must be taken in the interpretation of results. The presence of energy at 0 s on the k = 1 is indicative of dipping layers (Schulte-Pelkum and Mahan, 2014b; Liu et al., 2015) and can be used to identify which stations are possibly affected by complex geometries.

Appendix C. Supplementary data

Supplementary data associated with this article can be found, in the online version, at http://dx.doi.org/10.1016/j.pepi.2018.01.012.

References

Akiman, O., Erler, A., Göncüoğlu, M.C., Gülec, N., Geven, A., Türeli, K., Kadioğlu, Y.K., 1993. Geochemical characteristics of granitoids along the western margin of the Central Anatolian Crystalline Complex and their tectonic implications. Geol. J. 28, 371–382.

Audet, P., 2015. Layered crustal anisotropy around the San Andreas Fault near Parkfield, California. J. Geophys. Res. Solid Earth 120, 1–17. http://dx.doi.org/10.1002/2014JB011821.

Beck, S., Zandt, G., 2005. Continental Lithospheric Deformation along a Major Strike-slip Fault Zone: The Central North Anatolian Fault Zone. International Federation of Digital Seismograph Networks. Other/Seismic Network, Turkey 10.7914/SN/YL_2005.

Ben-Zion, Y., Sammis, C.G., 2003. Characterization of fault zones. Pure Appl. Geophys. 160, 677–715.

Bianchi, I., Park, J., Piana Agostinetti, N., Levin, V., 2010. Mapping seismic anisotropy using harmonic decomposition of Receiver Functions: an application to Northern Apennines, Italy. J. Geophys. Res. 115 (B12317). http://dx.doi.org/10.1029/2009JB007061.

Bianchi, I., Bokelmann, G., Shiomi, K., 2015. Crustal anisotropy across northern Japan. J. Geophys. Res. Solid Earth 120, 4998–5012. http://dx.doi.org/10.1002/2014JB011681.

Bianchi, I., Lucente, F.P., Di Bona, M., Govoni, A., Piana Agostinetti, N., 2016. Crustal structure and deformation across a mature slab tear zone: the case of southern Tyrrhenian subduction (Italy). Geophys. Res. Lett. 43, 12380–12388. http://dx.doi.org/10.1002/2016GL070978.

Biryol, C.B., Zandt, G., Beck, S.L., Özacar, A., Adiyaman, H.E., Gans, C.R., 2010. Shear wave splitting along a nascent plate boundary: the North Anatolian Fault Zone. Geophys. J. Int. 1, 1201–1213. http://dx.doi.org/10.1111/j.1365-246X.2010.04576.x.

Boness, N., Zoback, M., 2006. A multiscale study of the mechanism controlling shear velocity anisotropy in the San Andreas Fault Observatory at depth. Geophysics 71 (5), F131–F146.

Brownlee, S.J., Schulte-Pelkum, V., Raju, A., Mahan, K., Condit, C., Orlandini, O.F., 2017. Characteristics of deep crustal seismic anisotropy from a compilation of rock elasticity tensors and their expression in receiver functions. Tectonics 36, 1835–1857. http://dx.doi.org/10.1002/2017TC004625.

Bulut, F., Ben-Zion, Y., Bohnhoff, M., 2012. Evidence for a bimaterial interface along the Mudurnu segment of the North Anatolian Fault Zone from P-wave arrival times and polarization analysis. Earth Planet. Sci. Lett. 327–328, 17–22.

Çemen, I., Göncüoglu, M.C., Dirik, K., 1999. Structural evolution of the Tuz Gölü basin in central Anatolia, Turkey. J. Geol. 107, 693–706.

Cossette, É., Audet, P., Schneider, D., Grasemann, B., 2016. Structure and anisotropy of the crust in the Cyclades, Greece, using receiver functions constrained by in situ rock textural data. J. Geophys. Res. Solid Earth 121, 2661–2678. http://dx.doi.org/10.1002/2015JB012460.

Crampin, S., 1987. The geological and industrial implication of extensive dilatancy anisotropy. Nature 328, 491–496.

Çubuk-Sabuncu, Y., Taymaz, T., Fichtner, A., 2017. 3-D Crustal Velocity Structure of Western Turkey: constraints from full-waveform tomography. Phys. Earth Planet. Inter. (PEPI) 270, 90–112. http://dx.doi.org/10.1016/j.pepi.2017.06.014.

Dewey, J.F., Şengör, A.M.C., 1979. Aegean and surrounding regions: complex multiplate and continuum tectonics in a convergent zone. Geol. Soc. Am. Bull. 90, 84–92.

Di Bona, M., 1998. Variance estimate in frequency-domain deconvolution for teleseismic receiver function computation. Geophys. J. Int. 134, 634–646.

Eken, T., Bohnhoff, M., Bulut, F., Can, B., Aktar, M., 2013. Crustal anisotropy in the Eastern Sea of Marmara region in NW Turkey. Bull. Seismol. Soc. Am. 103 (2A), 911–924.

Fouch, M.J., Rondenay, S., 2006. Seismic anisotropy beneath stable continental interiors. Phys. Earth Planet. Inter. 158 (2), 292–320.

Girardin, N., Farra, V., 1998. Azimuthal anisotropy in the upper mantle from observations of P-to-S converted phases: application to southeast. Geophys. J. Int. 133, 615–629.

Göncüoğlu, M.C., 1977. Geology of Western Nigde Massif, PhD Thesis.

Görür, N., Tüysüz, O., Şengör, A.M.C., 1998. Tectonic evolution of the Central Anatolia Basin. Int. Geol. Rev. 40, 831–850.

Hurd, O., Bohnhoff, M., 2012. Stress and structural-induced shear-wave anisotropy along the 1999 Izmit Rupture, Northwest Turkey. Bull. Seismol. Soc. Am. 102 (5), 2177–2188. http://dx.doi.org/10.1785/0120110270.

Karasözen, E., Özacar, A.A., Biryol, C.B., Beck, S.L., 2014. Seismicity, focal mechanisms and active stress field around the central segment of the North Anatolian Fault in Turkey. Geophys. J. Int. 196, 405–421.

Kaymakçı, N., Özçelik, Y., White, S.H., Van Dijk, P.M., 2009. Tectono-stratigraphy of the Çankırı Basin: late Cretaceous to early Miocene evolution of the Neotethyan Suture Zone in Turkey. Geol. Soc. London Spec. Pub 311, 67–106.

Kennett, B., Engdahl, E.R., 1991. Travel times for global earthquake location and phase identification. Geophys. J. Int. 105, 429–465.

Kern, H., Wenk, H.R., 1990. Fabric-related velocity anisotropy and shear-wave splitting in rocks from the Santa Rosa Mylonite Zone, California. J. Geophys. Res. 95, 11213–11224.

Ketin, İ., 1966. Anadolu'nun Tektonik Birlikleri. M.T.A.Dergisi, vol. 66, pp. 20–34.

Kind, R., Eken, T., Tilmann, F., Sodoudi, F., Taymaz, T., Bulut, F., Yuan, X., Can, B., Schneider, F., 2015. Thickness of the lithosphere beneath Turkey and surroundings from S-receiver functions. Solid Earth 6 (3), 971.

Koçyiğit, A., 1991. An example of an accretionary forearc basin from northern Central Anatolia and its implications for the history of subduction of Neo-Tethys in Turkey. Geol. Soc. Am. Bull. 103, 22–36.

Langston, C.A., 1979. Structure of the Mount Ranier, Washington, inferred from teleseismic body waves. J. Geophys. Res. 84 (B9), 4749–4762.

Le Pichon, X., Kreemer, C., Chamot-Rooke, N., 2005. Asymmetry in elastic properties and the evolution of large continental strike-slip faults. J. Geophys. Res. 110. http://dx.doi.org/10.1029/2004JB003343.

Levin, V., Park, J., 1998. P-SH conversions in layered media with hexagonally symmetric anisotropy: a cookbook. Pure Appl. Geophys. 151 (2–4), 669–697.

Li, Z., Zhang, H., Peng, Z., 2014. Structure-controlled seismic anisotropy along the Karadere-Duzce branch of the North Anatolian Fault revealed by shear-wave splitting tomography. Earth Planet. Sci. Lett. 391, 319–326.

Licciardi, A., Piana Agostinetti, N., 2016. A semi-automated method for the detection of seismic anisotropy at depth via receiver function analysis. Geophys. J. Int. 205 (3), 1589–1612. http://dx.doi.org/10.1093/gji/ggw091.

Licciardi, A., Piana Agostinetti, N., 2017. Sedimentary basin exploration with receiver functions: seismic structure and anisotropy of the Dublin Basin (Ireland). Geophysics 82 (4). http://dx.doi.org/10.1190/geo2016-0471.1.

Liu, Z., Park, J., Rye, D.M., 2015. Crustal anisotropy in northeastern Tibetan Plateau inferred from receiver functions: rock textures caused by metamorphic fluids and lower crust flow? Tectonophysics 661, 66–80. http://dx.doi.org/10.1016/j.tecto.2015.08.006.

Lucifora, S., Cifelli, F., Rojay, B., Mattei, M., 2013. Paleomagnetic rotations in the Late Miocene sequence from the Çankırı Basin (Central Anatolia, Turkey): the role of strike–slip tectonics. Turkey J. Earth Sci. 22, 778–792.

Mainprice, D., Le Page, Y., Rodgers, J., Jouanna, P., 2007. Predicted elastic properties of the hydrous D phase at mantle pressures: implications for the anisotropy of subducted slabs near 670-km discontinuity and in the lower mantle. Earth Planet. Sci. Lett. 259, 283–296.

Maupin, V., Park, J., 2007. Theory and observations: wave propagation in anisotropic media. Elsevier, New York, pp. 289–321.

McClusky, S., et al., 2000. Global positioning system constraints on plate kinematics and dynamics in the eastern Mediterranean and Caucasus. J. Geophys. Res. 105, 5695–5719. http://dx.doi.org/10.1029/1999JB900351.

McClusky, S.C., Reilinger, R., Mahmoud, S., Ben Sari, D., Teableb, A., 2003. GPS constrains on Africa (Nubia) and Arabia plate motions. Geophys. J. Int. 155, 126–138.

Najdahmadi, S., Bohnhoff, M., Ben-Zion, Y., 2016. Bimaterial interfaces at the Karadere segment of the North Anatolian Fault, northwestern Turkey. J. Geophys. Res. 121 (2), 931–950.

Okay, A.I., 1996. Granulite facies gneisses from the Pulur region, Eastern Pontides. Turkish J. Earth Sci. 5, 55–61.
Okay, A., Tüysüz, O., 1999. Tethyan sutures of northern Turkey. Geol. Soc. London Spec. Pub. 156, 475–515. http://dx.doi.org/10.1144/GSL.SP.1999.156.01.22.
Olugboji, T.M., Park, J., 2016. Crustal anisotropy beneath Pacific Ocean-Islands from harmonic decomposition of receiver functions. Geochem. Geophys. Geosyst. 17, 810–832. http://dx.doi.org/10.1002/2015GC006166.
Özacar, A.A., Biryol, C.B., Zandt, G. and Beck, S.L., 2010. Deep Structure of Continental Strike-slip Faults Imaged by Receiver Functions, European Geophysical Union General Assembly 2010; 02–07 May 2010, Vienna, Austria.
Ozakin, Y., Ben-Zion, Y., Aktar, M., Karabulut, H., Peng, Z., 2012. Velocity contrast across the 1944 rupture of the North Anatolian fault east of Ismetpasa from analysis of teleseismic arrivals. Geophys. Res. Lett. 39 (L08307). http://dx.doi.org/10.1029/2012GL051426.
Park, J., Levin, V., 2016. Anisotropic shear zones revealed by back-azimuthal harmonics of teleseismic receiver functions. Geophys. J. Int. 207, 1216–1243.
Peng, Z., Ben-Zion, Y., 2004. Systematic analysis of crustal anisotropy along the Karadere-Duzce branch of the North Anatolian fault. Geophys. J. Int. 159, 253–272.
Piana Agostinetti, N., Chiarabba, C., 2008. Seismic structure beneath Mt Vesuvius from receiver function analysis and local earthquakes tomography: evidences for location and geometry of the magma chamber. Geophys. J. Int. 175 (3), 1298–1308.
Piana Agostinetti, N., Bianchi, I., Amato, A., Chiarabba, C., 2011. Fluid migration in continental subduction: the Northern Apennines case study. Earth Planet. Sci. Lett 10.1016/j.epsl.2010.10.039.
Piana Agostinetti, N., Malinverno, A., 2017. Assessing uncertainties in high-resolution, multi-frequency receiver function inversion: a comparison with borehole data. Geophyiscs in press.
Piana Agostinetti, N., Miller, M.S., 2014. The fate of the downgoing oceanic plate: insight from the Northern Cascadia subduction zone. Earth Planet. Sci. Lett. 408, 237–251. http://dx.doi.org/10.1016/j.epsl.2014.10.016.
Piana Agostinetti, N., Licciardi, A., Piccinini, D., Mazzarini, F., Musumeci, G., Saccorotti, G., Chiarabba, C., 2017. Discovering geothermal supercritical fluids: a new frontier for seismic exploration. Sci. Rep. 7, 14592. http://dx.doi.org/10.1038/s41598-017-15118-w.
Porter, R., Zandt, G., McQuarrie, N., 2011. Pervasive lower-crustal seismic anisotropy in Southern California: evidence for underplated schists and active tectonics. Lithosphere 3 (3), 201–220.
Reilinger, R., McClusky, S., Vernant, P., Lawrence, S., Ergintav, S., Çakmak, R., Ozener, H., Kadirov, F., Guliev, I., Stepanyan, R., Nadariya, M., Hahubia, G., Mahmoud, S., Sakr, K., ArRajehi, A., Paradissis, D., Al-Aydrus, A., Prilepin, M., Guseva, T., Evren, E., Dmitrotsa, A., Filikov, S.V., Gomez, F., Al-Ghazzi, R., Karam, G., 2006. GPS constraints on continental deformation in the Africa-Arabia, Eurasia continental collision zone and implications for the dynamics of plate interactions. J. Geophys. Res. Solid Earth 111, B05411.
Rojay, B., 2013. Tectonic evolution of the Cretaceous Ankara Ophiolitic Mélange during the Late Cretaceous to pre-Miocene interval in Central Anatolia, Turkey. J. Geodyn. 65, 66–81.
Rümpker, G., Kaviani, A., Latifi, K., 2014. Ps-splitting analysis for multilayered anisotropic media by azimuthal stacking and layer stripping. Geophys. J. Int. 199, 146–163.
Savage, M.K., 1998. Lower crustal anisotropy or dipping boundaries? Effects on receiver functions and a case study in New Zealand. J. Geohys. Res. 103 (15), 69–87.
Sayers, C.M., 1994. The elastic anisotropy of shales. J. Geophys. Res. 99, 767–774.
Schulte-Pelkum, V., Mahan, K.H., 2014a. Imaging faults and shear zones using receiver functions. Pure Appl. Geophys. 171 (11), 2967–2991. http://dx.doi.org/10.1007/s00024-014-0853-4.
Schulte-Pelkum, V., Mahan, K.H., 2014b. A method for mapping crustal deformation and anisotropy with receiver functions and first results from USArray. Earth Planet. Sci. Lett. 402, 221–233.
Şengör, A.M.C., 1979. North Anatolian Fault: its age, offset and tectonic significance. J. Geol. Soc. London 136, 269–282.
Şengör, A.M.C., Yilmaz, Y., 1981. Tethyan evolution of turkey: a plate tectonic approach. Tectonophysics 75, 181–241.
Şengör, A.M.C., Tüysüz, O., İmren, C., Sakınç, M., Eyidoğan, H., Görür, N., Le Pichon, X., Rangin, C., 2005. The North Anatolian Fault: a new look. Annu. Rev. Earth Planet. Sci. 33 (1), 37–112.
Seyitoğlu, G., Kazancı, N., Karadenizli, L., Şen, Ş., Varol, B., Saraç, G., 2004. Neogene tectono-sedimentary development of western margin of Çankırı basin, central Turkey: reply to the comment of Kaymakçı 2003. Terra Nova 16, 163–165.
Sherrington, H.F., Zandt, G., Frederiksen, A., 2004. Crustal fabric in the Tibetan Plateau based on waveform inversion for seismic anisotropy parameters. J. Geophys. Res. 109 (B02312), 376.
Shiomi, K., Park, J., 2008. Structural features of the subducting slab beneath the Kii Peninsula, central Japan: seismic evidence of slab segmentation, dehydration, and anisotropy. J. Geophys. Res. 113, 1–13. http://dx.doi.org/10.1029/2007JB005535.
Tadokoro, K., Ando, M., Baris, S., Nishigami, K., Nakamura, M., Ucer, S.B., Ito, A., Honkura, Y., Isikara, A.M., 2002. Monitoring of fault healing after the 1999 Kocaeli, Turkey, earthquake. J. Seiso-mol. 6, 411–417.
Tarayoun, A., Audet, P., Mazzotti, S., Ashoori, A., 2017. Architecture of the crust and uppermost mantle in the northern Canadian Cordillera from receiver functions. J. Geophys. Res. Solid Earth 122. http://dx.doi.org/10.1002/2017JB014284.
Taymaz, T., Jackson, J.A., Westaway, R., 1990. Earthquake mechanisms in the Hellenic Trench near Crete. Geophys. J. Int. 102, 695–731.
Taymaz, T., Jackson, J., McKenzie, D., 1991. Active tectonics of the north and central Aegean sea. Geophys. J. Int. 106, 433–490.
Taymaz, T., Westaway, R., Reilinger, R., 2004. Active faulting and crustal deformation in the Eastern Mediterranean region. Tectonophysics 391 (1–4), 375. http://dx.doi.org/10.1016/j.tecto.2004.07.005.
Taymaz, T., Yılmaz, Y., Dilek, Y., 2007a. The geodynamics of the Aegean and Anatolia: introduction. Geol. Soc. London Spec. Pub. 291, 1–16. http://dx.doi.org/10.1144/SP291.1.
Taymaz, T., Wright, T., Yolsal, S., Tan, O., Fielding, E., Seyitoglu, G., 2007b. Source characteristics of June 6, 2000 Orta-Çankırı (Central Turkey) Earthquake: a synthesis of seismological, geological and geodetic (InSAR) observations, and internal deformation of Anatolia Plate. Geol. Soc. London Spec. Pub. 291, 259–290. http://dx.doi.org/10.1144/SP291.12.
Vanacore, E., Taymaz, T., Saygin, E., 2013. Moho structure of the Anatolian Plate from receiver function analysis. Geophys. J. Int. 193 (1), 329–337.
Vinnik, L.P., 1977. Detection of waves converted from fPg to fSVg in the mantle,. Earth Planet. Lett. 15, 39–45.
Vinnik, L., Oreshin, S., Erduran, M., 2016. Melt in the mantle and seismic azimuthal anisotropy: evidence from Anatolia. Geoph. J. Int. 205, 523–530. http://dx.doi.org/10.1093/gji/ggw021.
Whitney, D.L., Hamilton, M.A., 2004. Timing of high-grade metamorphism in central Turkey and the assembly of Anatolia. J. Geol. Soc. London 161, 823–828.
Yolsal-Çevikbilen, S., Taymaz, T., 2012. Earthquake source parameters along the hellenic subduction zone and numerical simulations of historical tsunamis in the eastern mediterranean. Tectonophysics 536–537, 61–100. http://dx.doi.org/10.1016/j.tecto.2012.02.019.
Yolsal-Çevikbilen, S., Biryol, C.B., Beck, S., Zandt, G., Taymaz, T., Adiyaman, H.E., Özacar, A.A., 2012. 3-D crustal structure along the North Anatolian Fault Zone in north central Anatolia revealed by local earthquake tomography. Geophys. J. Int. 188, 819–849. http://dx.doi.org/10.1111/j.1365-246X.2011.05313.x.
Zhang, Z., Schwartz, S.Y., 1994. Seismic anisotropy in the shallow crust of the Loma Prieta segment of the San Andreas Fault System. J. Geophys. Res. 99, 9651–9661.
Zinke, J., Zoback, M.D., 2000. Structure-related and stress-induced shear-wave velocity anisotropy: observations from microearthquakes near the Calaveras fault in central California. Bull. Seismol. Soc. Am. 90 (5), 1305–1312.

Table S1: Summary of results. $E(n)$ is the energy as defined in the main text as a function of depth. S defines the three discrete depth ranges analysed in the main text. Negative values of $E(n)$ indicate a dominant contribution of the unmodelled component. Strike is not calculated in these cases.

Station	Lon. (deg)	Lat. (deg)	$S = 0 - 15$ km $\sum_{n \in S} E(n)$	Strike (deg)	Strike σ (deg)	$S = 15 - 30$ km $\sum_{n \in S} E(n)$	Strike (deg)	Strike σ (deg)	$S = 30 - 60$ km $\sum_{n \in S} E(n)$	Strike (deg)	Strike σ (deg)
ALIC	33.4870	40.9780	1.9563	45.5	1.82	0.6629	20.3	2.44	0.3211	5.2	2.96
ALIN	32.8790	41.0610	1.2253	69.7	1.21	-0.0066	–	–	-0.1223	–	–
ALOR	32.8700	41.3010	0.2909	20.8	1.88	0.1766	-13.1	6.10	0.0736	4.6	2.75
ARSL	35.8870	40.9550	0.3828	-4.2	7.02	0.2091	-69.8	6.87	0.2805	10.1	2.85
BAGB	36.4100	40.2780	0.2423	18.5	2.79	0.6541	-56.9	18.83	0.5134	-61.6	1.68
BEDI	33.5060	41.1210	0.0860	17.1	9.53	0.1854	-56.8	1.88	0.7994	49.1	2.31
BEKI	34.2630	41.3150	0.2944	-44.9	0.72	0.3657	8.8	3.08	0.4611	53.6	0.79
BOKE	36.2110	40.5520	0.4889	-42.5	18.37	0.4372	-49.7	3.43	0.8331	-30.2	23.88
CAKM	37.3670	40.0150	0.6062	27.6	2.19	0.8496	-54.4	2.90	0.3409	22.2	2.72
CALT	35.1250	41.3280	0.1942	40.6	3.86	0.3660	3.7	3.05	0.5115	46.5	1.70
CAYA	34.2690	40.3730	0.9903	11.0	0.61	0.1075	-4.3	5.68	0.7204	31.5	0.76
CRLU	34.3570	40.0640	0.2142	9.5	1.63	0.0704	-5.9	2.89	0.0667	-10.7	3.82
CUKU	33.4410	40.6040	0.8943	-6.7	1.66	0.1341	17.5	3.25	-0.0010	–	–
DERE	35.0640	41.4770	0.2923	-68.5	1.71	0.4796	47.8	1.70	0.3719	-41.8	3.09
DOGL	35.2840	40.3910	1.5613	32.3	9.82	0.7767	75.6	0.80	0.8728	44.6	1.38
DUMA	35.1400	40.9180	0.8905	31.5	1.86	0.3243	-3.6	1.07	0.1841	-37.9	2.03
EKIN	35.7870	41.1470	0.1748	23.6	0.78	0.4074	-23.2	4.27	0.1924	-3.7	1.96
GOCE	34.3480	39.7430	1.1026	-53.4	1.54	0.0715	-21.0	11.28	0.5318	-25.7	7.52
HASA	33.5650	41.4690	0.2054	16.5	3.69	0.0678	-23.5	8.24	0.1701	44.7	2.32
INCE	32.9060	40.5810	0.2247	-12.5	4.26	0.2696	-8.1	6.57	0.0303	25.7	3.92
INSU	35.3660	39.8420	0.1645	16.0	6.15	0.2326	57.6	1.02	0.2675	8.5	5.86
ISKE	37.0670	40.7640	0.1889	-9.5	11.55	0.0411	-30.5	1.92	0.1449	-54.9	1.99
KARA	35.2450	40.6880	0.2867	56.7	1.65	0.1418	-53.5	1.67	0.2099	30.7	2.26
KAVA	32.8780	40.2800	0.5120	1.0	2.31	0.4696	-16.8	2.58	0.2309	26.4	2.86
KGAC	34.3230	40.9410	0.4714	50.7	1.05	0.3590	40.4	4.47	0.0944	-8.7	2.52
KIYI	35.3160	40.1310	0.2481	-11.4	4.17	0.0861	-24.2	5.44	0.4505	2.8	4.45
KIZIK	36.5360	40.0480	0.6375	8.5	2.93	0.1492	48.7	1.16	0.1817	-56.2	5.35
KUYL	34.3320	41.5900	0.2564	58.3	2.16	0.5218	70.0	1.42	0.2875	56.2	0.83
KUZA	36.2480	40.4410	1.2193	63.2	2.02	0.5847	12.8	4.20	0.4626	-48.4	4.32
KUZO	32.8610	40.9040	2.1767	71.7	1.50	0.0489	-15.7	2.09	0.3306	22.6	3.26
OGUR	35.1650	41.1090	0.6163	-43.4	0.72	0.0359	7.0	0.32	-0.1154	–	–
PANC	34.3010	40.6470	0.1510	59.6	1.16	0.0510	46.4	1.28	0.3674	-48.4	1.95
PELI	34.2990	41.1130	0.7563	71.6	0.62	0.3513	49.3	3.12	0.6523	33.8	1.90
SEYH	32.9000	40.8560	2.7716	-62.1	3.64	1.0911	-61.9	4.17	0.1933	-6.4	1.83
SYUN	33.5290	40.8380	0.4143	6.8	4.58	0.5396	-9.4	2.28	1.4554	20.2	2.26
TEPE	35.7430	41.3690	0.3915	-16.2	4.10	0.2471	27.1	0.89	0.0290	37.2	1.64
YESI	37.2290	40.4050	0.9143	-70.1	2.07	0.8419	-39.3	3.09	0.2572	-63.3	1.99
YIKI	35.9540	40.7480	0.4725	-12.8	6.09	0.3004	-45.6	5.74	0.3351	-48.2	2.03